**Technical Memorandum**                                                        **AV10-018t**
To: Atmospheric Optics Group                                                  12 August 2010
From: J. E. Shields
Subject:  Theory of Operations for the MSI and Results of the Previous Contract

In documenting the data processing of the MSI and SRI data, I am finding that it would be very helpful to have a memo that documents the current algorithms and their inputs.  This memo in turn would benefit from a memo that documents the theory of operations, as well as the results from the previous project that used a black box at the other end of the path.  The theory and results of the previous experiment were written up in 2009, with the intent that the document be used in a final report on the previous project (to be written by our sponsors).  For the sake of convenience, in this memo I have copied the final draft of the chapter below.

This chapter documents the results of the work when the project ended in approximately June 2007.  At that point, we had used the MSI looking in a single direction, and with a black box at the other end of the path.  The current grant is to explore the impact of extending these concepts to look in all directions, to use available targets of interest such as the horizon contrast, and to provide results in the Near InfraRed.  In an additional memo, AV10-020t, I will provide an overview of the current MSI and SRI algorithms and their inputs.

# Chapter 9.  Multispectral Scattering Imager

Janet E. Shields, Richard W. Johnson, Justin G. Baker, Monette E. Karr, and Art R. Burden

Marine Physical Laboratory, University of California San Diego, La Jolla CA 92093-0701

and

Paul J. Berger

Massachusetts Institute of Technology, Lincoln Laboratory, Lexington, MA 02420

## 9.1 Introduction

The objective of this part of the program was to develop an instrumented version of a visibility sensor and determine whether the instrument can provide reliable integrated-path measurements of the extinction coefficient.  A visibility measurement (more properly a contrast-based measurement) requires a sensor at one end of the path and a passive reference target at the other end of the path.  This single-ended measurement is much easier to implement than a transmission measurement, which requires attention to instruments at both ends of the path.

Visibility measurements are often made in atmospheric measurement programs.  In its most simple form, an observer looks for large black objects at known distances seen against the horizon sky and selects an object which is just discernable.  The extinction coefficient in the photopic band is determined from this visual range by Koschmeider's formula, $\alpha = 3.912/VR$ [Ref. 9-1].  The equation $\alpha = 3.0/V$, where V is Visibility, rather than visual range, is also in common use.   In practice, many ranges do not have an adequate number of objects at known distances and selecting the barely discernable object is somewhat subjective.  Various instruments have been built to overcome these limitations, for instance, the optical pyrometer used in the NRL experiments [Ref. 9-2] and teleradiometers [Ref. 9-3] used in the air quality monitoring programs in the national parks.  Measurements with these instruments require skilled operators and are not suitable for long-term unattended operation.

The University of California San Diego (UCSD) Marine Physical Laboratory (MPL) developed a new instrument for this program, with the goals of providing accurate measurements with an instrument capable of unattended operation.  This instrument, called a Multispectral Scattering Imager (MSI), was based on UCSD's extensive experience in building and operating a Horizon Scanning Imager (HSI) for extended path visibility measurements and Whole Sky Imagers (WSI) for cloud cover measurements [Refs. 9-4 – 9-10].  The MSI was designed to acquire calibrated radiance images in four wavelength bands over extended paths.  From measurements of the horizon radiance and the radiance of dark targets, combined with measurements of the inherent properties of the dark targets, visibility and effective scattering coefficient over the integrated path can be determined.

## 9.2  Theory of Operation

A rigorous set of equations describing the operation of the MSI is given by Shields [Ref. 9-11]. Because there is often confusion between the definitions of radiance, irradiance, illuminance, and similar terms, as well as confusion regarding which parameters decrease with distance squared and which do not, we would like to go back to a more basic discussion

in this chapter.  If the reader is familiar with these terms, skip to Section 9.2.2, which discusses how the equations are used in the MSI system.

9.2.1  Basic Definitions

As discussed in Boyd [Ref 9-12], McCluney [Ref 9-13] and others, a source radiating energy or flux dφ into a solid angle dΩ has a radiant intensity I in a given direction defined by I = dφ/ dΩ.  Boyd shows that if the source has an area given by dA, then the irradiance of this source, as seen from a distance r and angle θ is given by

$$E = \frac{d\phi}{dA} = \frac{I \cos\theta}{r^2}$$  9.1

Boyd also shows that the inverse-square law, i.e. the $1/r^2$ term, in general is valid only for the irradiance of point sources, where the source is much smaller than the sensor field of view.  The term irradiance may be taken as the energy per unit area emitted by a radiant source.  It can also be taken as the energy per unit area received by a diffuse surface.  We note here that spectral irradiance refers to the irradiance per waveband, integrated over a source and sensor effective waveband.  When this waveband is specifically the responsivity of the human eye, the illuminance can be derived, as discussed in Boyd and McCluney.

Boyd also defines the related term radiance as the energy per unit area per unit solid angle emitted by a radiant source, and shows that it can be defined by the equation

$$L = \frac{d^2\phi}{dA \cos\theta d\Omega}$$  9.2

In this equation the cosθ term comes from the fact that we are talking about a source of area dA, but when viewed from an angle θ, its effective area is cosθ dA.  More generally, if a sensor such as a photometer views any extended source that fills the field of view of the photometer, we define the radiance as the energy per unit area per solid angle received by the photometer.  Similarly, with an imaging system such as a camera with a lens, if no diffuser is present in the system, and the extended source is large enough to fill a pixel, then the signal of that pixel is related to the radiance, or radiant energy per unit area of the sensor per solid angle of the pixel.  That is, each pixel acts like a photometer, and measures radiance, not irradiance. (The irradiance of a point source can be determined from these measurements in a calculation that includes integrating over the point spread function of the sensor, but we do this only for stars or other point sources.)

The spectral radiance refers to the radiance normalized over the source and sensor waveband, and luminance refers to the luminous flux per area per solid angle, much like illuminance refers to luminous flux per area.  The path along which the radiance travels may be called either the line of sight or the path of sight.

We also note that the signal for a given pixel produced by an imaging system is well related to the radiance of the portion of the scene corresponding to each pixel, if the sensor can be carefully calibrated (some cameras have characteristics such as automatic gain that can preclude this).  In the absence of calibration corrections, sensor signals are often poorly related to the radiance.  This will be discussed in a later section, but for now it is sufficient to

note that we have calibrated our sensor signals so that they are well related to the relative spectral radiance of the scene seen by each pixel.

One of the basic laws of radiometry is that in the absence of atmospheric losses, and with uniform index of refraction, radiance is conserved. The radiance of an extended source as viewed from distance $r_1$ is the same as the radiance as viewed from distance $r_2$, where by definition the extended source must fill the field of view of the pixel at both distances. This law that radiance is conserved is also derived in Boyd. From an intuitive point of view, one can think of a simple photometer or Gershun tube, i.e. a tube with a sensitive area dA and solid angle dΩ. As the distance r of this tube to an extended source is increased, the amount of flux received from any point on the source decreases by $1/r^2$, however the total area seen by the sensor increases by $r^2$, so that the radiance seen by the sensor remains constant in the absence of atmospheric attenuation and scattering.

Attenuation is sometimes defined as the loss of irradiance in an incremental path if and only if the light is collimated [McCartney Ref 9-14]. Since we are working with radiances, we prefer to define attenuation as the loss of radiance in an incremental path as in Duntley [Ref 9-15] and Liou [Ref 9-16].

$$\Delta L / L = \alpha dr = \alpha dz \sec \theta \qquad\qquad 9.3$$

In this equation, L is radiance, $\alpha$ is attenuation, r is distance along the path, z is altitude, and $\theta$ is the angle from the vertical. If we are dealing with spectral radiance, then typically radiance is in the units of watt/ster $m^2$ μm, z and r can be given in m or km, and $\alpha$ has the units of $m^{-1}$ or $km^{-1}$.
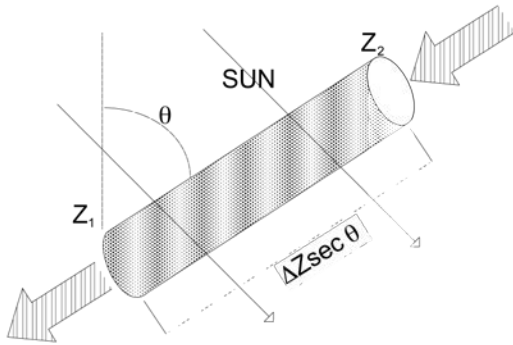


Fig. 9-1. Light attenuation and scattering in the incremental path

In addition, light is scattered into the incremental path from the surround. Thus in the presence of an atmosphere, the incremental radiance change is

$$\Delta L / \Delta z \sec \theta = L_* (z, \theta, \phi) - L(z, \theta, \phi) \alpha \qquad\qquad 9.4$$

In this equation $L_*$ is the path function, which is the light scattered from the sun, sky, and terrain, into the direction of the path of sight by the atmosphere in the incremental volume. We next define the radiance of a target at range 0 as inherent radiance, defined as

$$_t L_0 (z_t, \theta, \phi) \qquad\qquad 9.5$$

where $z_t$ is the altitude of the target. Similarly, the radiance of a target at range r is called the apparent radiance

$$_t L_r(z, \theta, \phi) \qquad\qquad 9.6$$

where z is the altitude from which the target is observed.

Integrating the equation of transfer 9.4, we can derive that these terms are related by the equation

$$_t L_r(\theta, \phi) = {_t}L_0(\theta, \phi) * T_r(\theta) + {_p}L_r^*(\theta, \phi) \qquad\qquad 9.7$$

In this equation, Tr is the beam transmittance of the path, defined by

$$T_r(\theta) \equiv e^{-\alpha r} \qquad\qquad 9.8$$

Note that the $\phi$ term has disappeared, because in a reasonably uniform atmosphere, the transmittance is not dependent on the azimuth angle. This term represents the loss in image-forming light over the full path.

In the equation, the $_p L_r^*(\theta, \phi)$ term is called the path radiance, and is defined as

$$_p L_r^*(\theta, \phi) \equiv \int_0^r L_*(\theta, \phi) T_{ri}(\theta) dr \qquad\qquad 9.9$$

In this equation, $T_{ri}(\theta)$ is the transmittance from the observer to the range of the incremental path. That is, we integrate the path function over the whole path, taking into account that the light scattered into any incremental path will be further attenuated by the path between the observer and the incremental path position.

Thus our integrated form of the equation of transfer Eq. 9.7 shows that the apparent radiance of a target is equal to the inherent radiance of the target times the transmittance from the observer to the target, plus the light scattered into the path from the surround for the whole path. The former term is the light with information about the target, and the latter term can be thought of as a noise term, as it has no information about the target.

All of these equations apply both to radiance and to monochromatic spectral radiance. We use reasonably narrow pass bands such that it also applies to the spectral radiance averaged over our passbands.

## 9.2.2. Derivation of Visibility and Extinction from the Measurements

This section develops the equations that provide the theoretical basis for the MSI. As discussed in Section 9.2.1, the apparent radiance $_t L_r$ of a visual target t, as observed from range r, is a function of the inherent radiance of the target measured from range 0, the beam transmittance $T_r$ of the path, and the path radiance $_p L_r^*$ over the path. The beam transmittance is a loss term, and represents the loss in radiant energy due to scattering and absorption (which together comprise attenuation). The path radiance is a gain term, however it contains no information about the target. It consists of the radiance scattered into the path of sight by the molecular, aerosol and other scattering components along the path.

All of these components are directionally dependent, as shown in Eq. 9.10, however the equation is often given in the form of Eq. 9.11 for notational convenience.

$$_t L_r(\theta,\phi) = {}_t L_0(\theta,\phi) * T_r(\theta) + {}_p L_r^*(\theta,\phi) \qquad\qquad 9.10$$

$$_t L_r = {}_t L_0 * T_r + {}_p L_r^* \qquad\qquad 9.11$$

The universal contrast is the contrast between the target and its background. Equation 9.12 shows the inherent contrast, measured from range 0; apparent contrast is represented by the same equation, with 0 replaced with range r.

$$C_0 = \frac{{}_t L_0 - {}_b L_0}{{}_b L_0} \qquad\qquad 9.12$$

Substituting Equation 9.11 into the version of Equation 9.12 for range r, we have

$$C_r = \frac{{}_t L_r - {}_b L_r}{{}_b L_r} = \frac{({}_t L_0 * T_r + {}_p L_r^*) - ({}_b L_0 * T_r + {}_p L_r^*)}{{}_b L_r} \qquad\qquad 9.13$$

At this point in the equation, we assume that the background is at the same place as the target, i.e. at the same range and also essentially adjacent to the target. In this case the path radiance over range r, from the viewer to the target, is the same as the path radiance over range r from the viewer to the background, and the path radiance terms cancel as in Eq. 9-14. In practice, we can use a background that is close enough to being adjacent so that the path radiances are the same. The impact of using the horizon for the background will be discussed later.

$$C_r = \frac{{}_t L_0 * T_r - {}_b L_0 * T_r}{{}_b L_r} \qquad\qquad 9.14$$

Now we can rearrange this equation as in Eq. 9.15, and substitute in Eq. 9.12 to yield Eq. 9.16.

$$C_r = \frac{T_r * ({}_t L_0 - {}_b L_0)}{{}_b L_r} = \frac{T_r * ({}_t L_0 - {}_b L_0)}{{}_b L_0} \frac{{}_b L_0}{{}_b L_r} \qquad\qquad 9.15$$

$$C_r = T_r * C_0 * \frac{{}_b L_0}{{}_b L_r} \qquad\qquad 9.16$$

Next consider the case where the background is in fact the horizon. In this case, $_b L_r$ is the horizon as seen from a distance r from the target. And $_b L_0$ is the horizon as seen from the position of the target. Duntley discusses the concept of equilibrium radiance. If a target is very bright, the radiance of a target will asymptotically decrease as r increases. If the target is very dark, the radiance of a target will asymptotically increase as r increases. All targets will asymptotically approach what's called the equilibrium radiance. Equilibrium radiance is the radiance for which the transmission losses over an incrementally small path are equal to the path radiance increases over an incrementally small path, so that there is no difference between the radiance when it enters the increment and leaves the increment.

Duntley shows that the clear horizon radiance in each direction along the horizon is equal to the equilibrium radiance in that direction. That is, in a uniform atmosphere, for a horizontal line of sight, the horizon radiance will have reached equilibrium, assuming it is not so clear that the earth curvature effects become significant. One caveat is that if there are clouds on the horizon, the measured horizon radiance will not equal the clear horizon radiance. However, if the clouds are far enough away that they cannot be detected as having

a signal different from the adjacent sky, then the radiance is at equilibrium, within measurement error.

As a result, if we use the horizon as our background, then $_b L_r$, i.e. the horizon as seen from a distance r from the target, is equal to $_b L_0$, the horizon as seen from the position of the target. These terms cancel in Eq. 9.16, yielding Eq. 9.17.

$$C_r = T_r * C_0 \qquad\qquad 9.17$$

Thus the assumptions that have gone into this equation are

a) The target background is the horizon

b) The angle to the horizon is close enough to the angle to the target that the equilibrium radiance will be the same, within measurement error.

c) The horizon is cloud-free. In practice, we check this by evaluating the standard deviation within a horizon region of interest in an image.

By definition, we also have the equations for transmittance given in Eq. 9-18.

$$T_r \equiv e^{-\alpha r} \qquad\qquad 9.18$$

where α is extinction coefficient. In the visible, the scattering coefficient s is, for all practical purposes, equivalent to the extinction coefficient α. Inserting Eq. 9.18 into 9.17, substituting s for α, and rearranging, we have

$$C_r = e^{-sr} * C_0 \qquad\qquad 9.19$$

$$s = -\frac{1}{r}\ln(C_r/C_0) \qquad\qquad 9.20$$

Visibility is typically defined as the range $r$ at which a large black target is just at threshold for a human viewer. The AMS Glossary of Meteorology [Ref 9-17] discusses this concept. Although the human contrast threshold depends on a number of parameters such as light adaptation and target shape, Duntley used ε = -.05 as a good rule of thumb when the human is looking at a large black target. Some researchers have found that -.02 may be a better number for the human contrast threshold, and this is why meteorological range is defined with a contrast of -.02. If the target is completely black, it has a radiance $_t L_o = 0$, and the inherent contrast, from Eq. 9-12, is

$$C_0 = \frac{(0-_b L_0)}{_b L_0} = -1 \qquad\qquad 9.21$$

Thus by substituting V for r in Eq 1, substituting a value of -.05 or ε for $C_r$, and substituting a value of -1 for $C_0$, we derive

$$\varepsilon = e^{-sV} * (-1) \qquad\qquad 9.22$$

which, when rearranged, becomes

$$s = -\frac{1}{V}\ln(-\varepsilon) \qquad\qquad \text{or} \qquad V \equiv -\ln(-\varepsilon)/s \qquad\qquad 9.23$$

This very simple equation becomes V = 3/s when a threshold of -.05 is used. Eq. 9.23 is in common usage, but it assumes that the human had a big object that was truly black, it was seen against a clear horizon, and it was at such a range that its apparent contrast was really at the human threshold. These are a lot of assumptions, and this is one reason why visibility determined by human estimation is often considered a rough estimate.

With the MSI, however, we do not have to make these same assumptions. We don't have to have the target at the threshold, because we can measure its apparent contrast. We

don't have to have the target exactly adjacent to the horizon, because we can measure the horizon separately (as long as it's at the same approximate angle). We don't have to have a completely black target, because we can measure most targets from close range or on clear days and estimate the inherent contrast. The definition of visibility is still the same, but by measuring the actual apparent and inherent contrast, we can determine the visibility more accurately. Substituting the definition of visibility, Eq, 9-23 into Eq 9.20 and rearranging, our equation for determining visibility from MSI measurements becomes

$$V = \frac{r * \ln(-\varepsilon)}{\ln(C_r/C_0)}$$

9.24

### 9.2.3. Application of these Equations with the MSI

To use this method, we measure the signal of a dark target from range r, and measure the nearby horizon. The signals are calibrated for relative radiance. Although it is beyond the scope of this report to provide details of this calibration, it can be noted that the calibration includes the following steps:

a) Correct for the dark signal, which is typically about 500 counts out of 65,535 and depends slightly on pixel as well as on exposure and CCD chip temperature.

b) Correct for the effective opening time of the shutter – this is actually done by setting the exposure time to account for this term, which is measured during calibrations.

c) Apply a linearity correction. Ideally, the dark-corrected signal should vary linearly with the input radiance. We measure the relationship, characterize it with a multi-term polynomial, and correct for the non-linearity.

d) Apply a uniformity correction. The absolute sensitivity of each pixel varies slightly, primarily due to Fresnel losses and other effects in the optics, and transmission losses in the fiber optic taper that transfers the image plane down to the CCD chip. The uniformity correction adjusts for these multiplicative factors.

Because the contrast is a ratio, it turns out that it is not necessary to calibrate to the absolute radiance level, which makes it more convenient and also avoids any impact due to absolute calibration errors. In some of our other systems, we calibrate for absolute radiance, but this system does not require it.

These calibrated signals are then used in the first half of Eq. 9-13 to directly determine the apparent contrast. Prior to deployment of the target, we similarly measured the inherent contrast, with the sensor in a parking lot a few feet from the target, but looking at the same angles as would be used during the experiment. The range r was also known, and this enables us to compute both the scattering coefficient and the visibility as defined in Eqs. 9.20 and 9.24. It should be noted that if there is significant absorption, the system will in fact measure attenuation coefficient, rather than scattering coefficient (i.e. in this case we do not substitute s for α in equation 9.20).

## 9.3 Equipment Description

The system, shown in Figure 9-2, includes a $512 \times 512$ 16-bit digital CCD camera, a filter changer, and a Sigma 170 – 500 mm zoom lens with a doubler. The filter changer has two filter wheels. One wheel contains four spectral filters: blue (450 nm), green (550 nm), red (650 nm), and NIR (800 nm). Each of the filters has a FWHM bandwidth of approximately 40 nm, although 70 nm filters were used in the initial experiments. The spectral width of the green filter is similar to the photopic band and we will refer to data

acquired with the green filter as the photopic band data. A second filter wheel contains neutral density filters that may be used to adjust the flux levels. Unlike the more common 24-bit color camera with 8-bit resolution in each color, this system has 16-bit (65,536 grey levels) in each spectral filter, as well as additional neutral density filters and exposure control for a useful dynamic range of over 10 logs or $10^{10}$. The experiments reported in this document were taken at f# 350 with a doubler, and the resulting image has a 2.25° field of view.



Figure 9-2. MSI sensor head, with zoom lens and 16-bit digital CCD camera

The measurements were made over a 7.07-km path across Zuniga Shoal, just outside San Diego bay. The black target and the shed containing the MSI sensor head and controller are shown in Figure 9-2. The black target consists of a hollow black box 8' on a side and 12' deep.



Figure 9-3. MSI installation at Zuniga Shoal: (right) shed containing sensor head at Ballast Point, and (left) black target at Naval Amphibious Base

The measured reflectance of the paint used for the target varied from 3.1% to 3.3% in the blue through the NIR wavelengths. The inherent contrast of the target with respect to the horizon was measured throughout two days at the angle of the line of sight of the experiment. The results are shown in Table 9-1. The results are quite close to –1, and relatively invariant as a function of time and spectral filter. The average values for each filter shown in Table 9-1 were used in the processing.

| Table 9-1.  Measured Inherent Contrast of the Target | | | | |
|---|---|---|---|---|
| Local Time | Blue | Green | Red | NIR |
| 0900 – 1030 | - 0.981 | - 0.979 | - 0.982 | - 0.988 |
| 1030 – 1145 | - 0.990 | - 0.987 | - 0.990 | - 0.993 |
| 1300 – 1430 | - 0.990 | - 0.988 | - 0.989 | - 0.992 |
| 1440 – 1535 | - 0.992 | - 0.991 | - 0.993 | - 0.994 |
| Average | - 0.988 | - 0.986 | - 0.988 | - 0.992 |

Figure 9-4(a) shows an image for a very clear day, often associated with Santa Ana wind conditions. Figure 9-4(b), extracted from Figure 9-4(a), shows the dark target (the black square above the sand.) The black target occupies approximately 5 × 5 pixels, of which we extract a 3 × 3 region for the visibility determination. The speckling that can perhaps be seen in this figure is due to the fiber optic taper, and is corrected in processing by the application of the uniformity calibration correction.



Figure 9-4(a). Image on 4 Dec 2005
V = 74 km, S = 0.04 km$^{-1}$

Figure 9-4(b). Zoomed image showing
black target (tip of arrow) at 7.07-km range

Figures 9-5 and 9-6 show sample imagery acquired with the green filter along with the extracted scattering coefficients and visibility results. Figure 9-5 shows an image for light haze. On this day, Los Coronados Islands in Mexico were clearly visible at 40-km range from Point Loma. Figures 9-6 and 9-7 show images for moderate haze and fog. It should also be noted that we have not shown the full dynamic range of the system in the images. The sensor has 65,535 grey levels, with a readout noise of 1 count (and a shot noise that depends on signal level). This high radiometric-resolution data is available for data processing and results in reasonable determinations even under fog conditions, when the target is not easily discerned in the image, as shown in Figure 9-7.
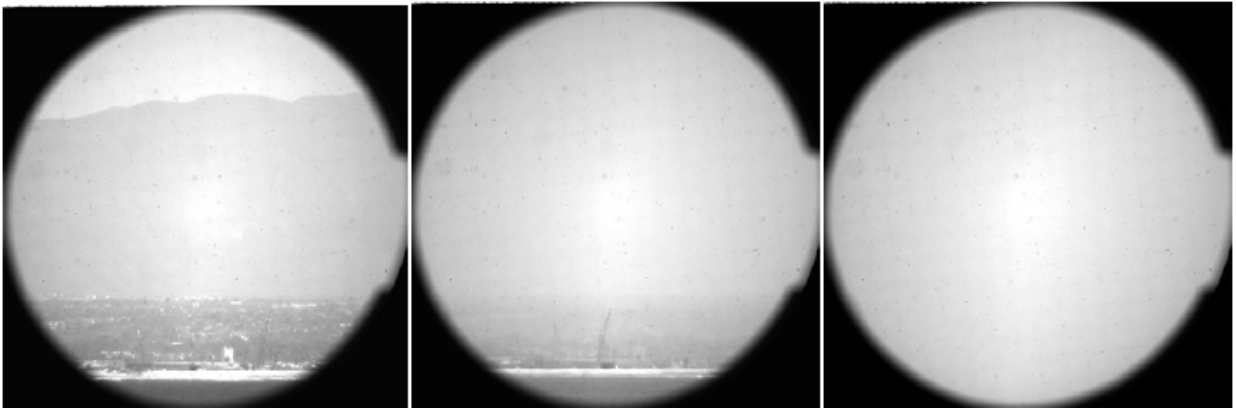


Figure 9-5.  30 Nov 2005          Figure 9-6.  17 Nov 2005          Figure 9-7.  30 Aug 2005

$V = 46$ km, $S = 0.066$ km$^{-1}$          $V = 29$ km, $S = 0.10$ km$^{-1}$          $V = 10$ km, $S = 0.30$ km$^{-1}$

Several factors that can influence the accuracy of the extinction measurements determined with the MSI. First, the inherent target contrast with respect to the horizon is an important input. We carefully measured this contrast in the direction of the path of sight from a range of a few feet prior to the deployment. As shown earlier, we found that the contrast was quite close to an ideal black target, with contrasts ranging from $-0.986$ to $-0.992$. The average value for the day was used for each filter, and the variation over the day was about 0.004. Although a perfect black target is not necessary for use with the MSI, earlier sensitivity studies showed that results are most accurate when the target contrast is reasonably dark, or when the inherent contrast is reasonably well known.

Second, image quality is important. The acquired images are corrected for the camera bias and dark levels. The system is carefully calibrated, and non-linearity corrections are made. The linearity calibration is defined as a correction to the relative signal change as a function of radiance change. At signals of 100 near the low end, the correction is about 2% with respect to a signal of 10,000, and at signals over 40,000 the correction is about 4% in the other direction, with the correction varying smoothly over the full measured range. We made a uniformity correction for the target and horizon extracted Region of Interest (ROI). The uniformity calibration is defined as a correction for pixel-to-pixel sensitivity differences in the image caused by lens, filter and CCD effects. Figure 9-8 shows an enlarged image of the target and regions around the target for a high extinction case ($\alpha_{Ext} \sim 0.3$ km$^{-1}$). The

specks in the imagery are due to the non-uniformity of the fiber optic taper used in this system. These are corrected for with the non-uniformity correction. Figure 9-9 shows an example of a partial uniformity correction.
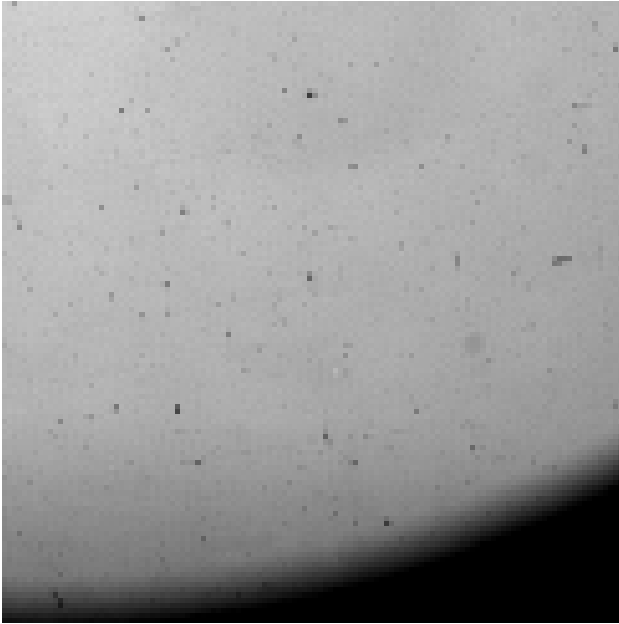


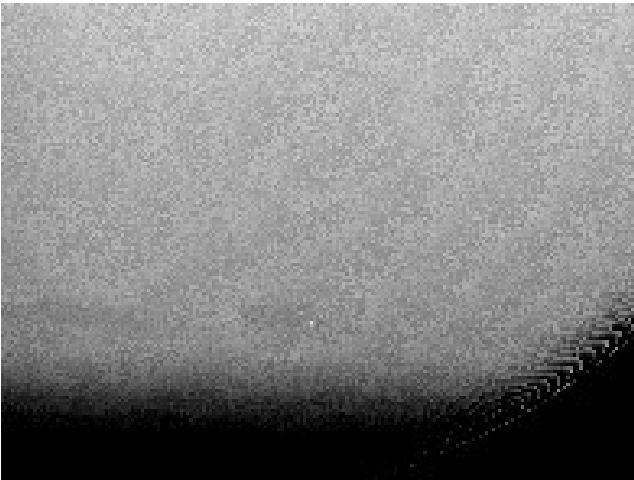Figure 9-8. Enlarged image of region around target, showing dark pixels due to fiber-optic taper



Figure 9-9. Enlarged image after application of integer non-uniformity correction

(The normal flat field correction is done at full resolution in floating point; this figure was a partial correction done with integers.) There is still some residual granularity in the image, showing that pixel-to-pixel non-uniformity correction is needed for accurate contrast measurements at high extinction. As mentioned earlier, the sensor has over 65,000 grey levels and a readout noise of about 1 count, so features are available to the algorithm that cannot be seen in the imagery. This is why the algorithm returns a non-zero visibility for these very foggy cases. The algorithm is taking advantage of the small, but significant, features in the numerical data,

to return a reasonable number even when the features are difficult to see in the imagery. We also investigated the effect of crosstalk on the light received from the target region. The target is right next to the highly reflective beach sand, and there may be an impact due to scattering of light (optical cross-talk) within the system. We measured cross talk, and experimented with corrections, but found that corrections did not appear to be necessary.

Third, in the derivation presented in Section 9.2, it was assumed that the atmospheric parameters and solar illumination are uniform over the path to the target and to the horizon. Occasionally the horizon was not at equilibrium radiance due to the presence of clouds. These cases were automatically detected and removed by evaluating the standard deviation of the corrected signals within the horizon ROI. Occasionally the program was not successful in its attempt to find the target, and these cases were automatically detected and removed by evaluating the STD (standard deviation) within the target ROI (region of interest used in the processing)

Fourth, the presence of boats in the line-of-sight to the target interferes with the measurements, attenuating the scattered light or, in some cases, providing a source of extraneous scatter. Out of the 5248 images from the August period, 56 had boats or ships in the line of sight to the target. These cases were detected visually and flagged and removed from the data set. Logic was added to the algorithm to automatically remove cases where either the target or the horizon region of interest (ROI) was off-scale, dark or bright. In the August 2005 data set, a total of 294 cases (5.6% of the data set) were detected and removed for one of the reasons described in the two paragraphs above.

Fifth, as shown in Figure 9-4, the line of sight to the "horizon" is somewhat higher than the line of sight to the target. Although the difference appears extreme in the imagery, the difference in angle is actually only 1.6 degrees. Figure 9-10 illustrates the geometry and shows how the terms used in calculating the scattered light received by the camera vary between a horizontal path and a slant path. We assume that the path function defined in Section 9.2.1 is composed of two terms: a direct component (fraction $f$) from the sun which increases with altitude and a component from the surrounding environment (upwelling radiation, multiple scattering from atmosphere) which is relatively constant with altitude in the boundary layer. We define the height of an increment of the slant path above the horizontal path to be $\Delta h$. And we assume that the extinction coefficient decreases with altitude exponentially, where we use the term hf to define the fold point, or height at which it has dropped by a factor of 1/e. There is a competition between the terms: at each incremental path region, the scattering will be lower at Δh, but the illumination will be higher at Δh, and the transmission to the camera will be higher due to the reduced extinction at Δh. This gives us the equations

$$\alpha(\Delta h) = \alpha(0)e^{-(\Delta h/hf)} \qquad\qquad 9.25$$

$$L_*(0) = f * L_*(0, direct) + (1-f) * L_*(0, diffuse) \qquad\qquad 9.26$$

$$L_*(\Delta h) = \frac{f * L_*(0, direct)}{T(\Delta h)} + (1-f) * L_*(0, diffuse) \qquad\qquad 9.27$$

These equations may be combined with those provided earlier to derive the impact of the slightly higher angle on the extinction calculation.
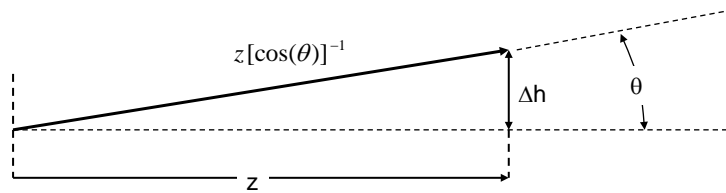
Figure 9-10.  Terms involved in calculating the received scattered light from a slant path and a horizontal path

We have evaluated the integral forms of Eqs 9.25 – 9.27 for the horizontal and slant paths to determine two values of $L_r^*$ to use in calculating the contrast ratio.  Figure 9-11 shows the results of a calcu-lation using the simple assumptions shown Figure 9-10, with $f = 0.25$ and an e-folding height of 2000 m.  This figure compares the extinction coefficients calculated using the $L_r'^*$ from the slant path versus $L_r^*$ from the horizontal path.  This plot shows an S-shape – the measured extinction coefficient is too high at the low end and too low at the high end using the slant path horizon.  For low extinction coefficients, more scattered light is received from the horizontal path than the slant path.  Contributions to the received light come from distant portions of the path as well as from nearby portions of the path.  For higher extinction coefficients, more light is received from the slant path than from the horizontal path and most of this light comes from the nearby portion of the path ( > 99 % within 10 km for an extinction coefficient of 0.5 $km^{-1}$).  The difference between the light from the slant path and the horizontal path is small (0.7 % for an extinction coefficient of 0.5 $km^{-1}$, but, for high extinction, the light from the path to the black object and the path to the horizon are almost equal and a small difference in the value used for the horizon has a proportionally larger effect.  The calculations presented here were intended to explore a possible source of error.  They suggest that there might be some effect due to the slant path.  More detailed calculations are needed to quantify this effect.
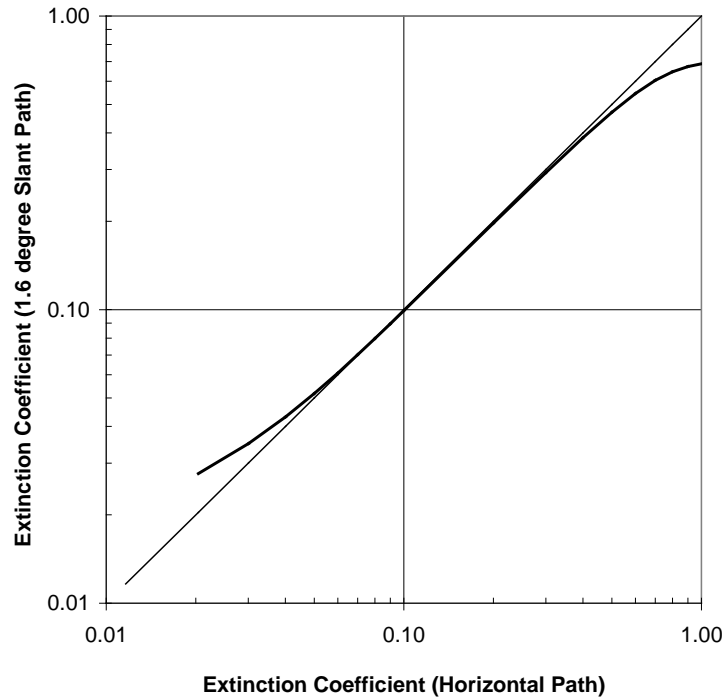
Figure 9-11.   Comparison of extinction coefficients determined with a slant path and a horizontal path.

## 9.4 Measurements

Data sets were acquired every 10 minutes 24 hours a day, and data sets were extracted from this, from approximately 8 am to 3 pm.  The system was extremely reliable.  In the first six months of operation, there was only one outage due to equipment failure.

Data sets were acquired in the original hardware configuration from 3 February 2005 to 20 July 2005.  Reference 9-11 describes the initial results from the winter and spring of 2005.  Improvements were made to the system in July 2005.  Measurements with the improved system were made from 1 August 2005 to 10 April 2006 and from 20 October 2006 to 10 December 2006.  The data acquired from August 2005 to December 2006 will be presented below.

Figure 9-12 shows a plot of the scattering coefficient at noon for every day in August 2005.  The variation from day to day is quite reasonable.  An evaluation of data shows a very good relation-ship between the appearance of the imagery and the extracted data.  For example, fog incidents can be seen in the imagery on days 241 and 242.  The spectral relationship is well behaved in the blue, photopic, and red, however the scattering coefficients appear to be slightly high in the NIR.  We believe that the NIR data are slightly offset, because the lens coating for this lens is not optimized for the NIR.  With 11 lenses in the zoom lens, the throughput of the lens is very sensitive to the coating properties.  Although a zoom lens was necessary for this developmental instrument, a better design for a field device would be a fixed lens with coatings optimized for the wavelengths in use.
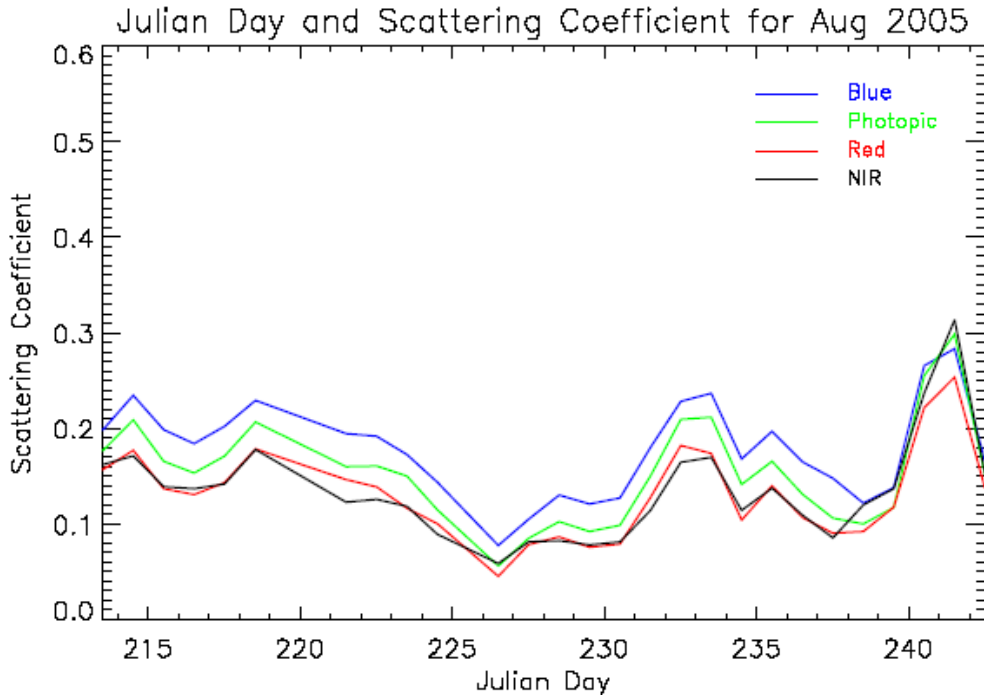
Figure 9-12.  Scattering coefficients measured at noon in August 2005

We also evaluated the results as a function of time of day, in order to evaluate whether there might be biases due to solar angle or other factors.  Figure 9-13 shows the variation during a period of 6 days in October 2005.  Day 295 shows a strong change during the day, as the atmosphere cleared.
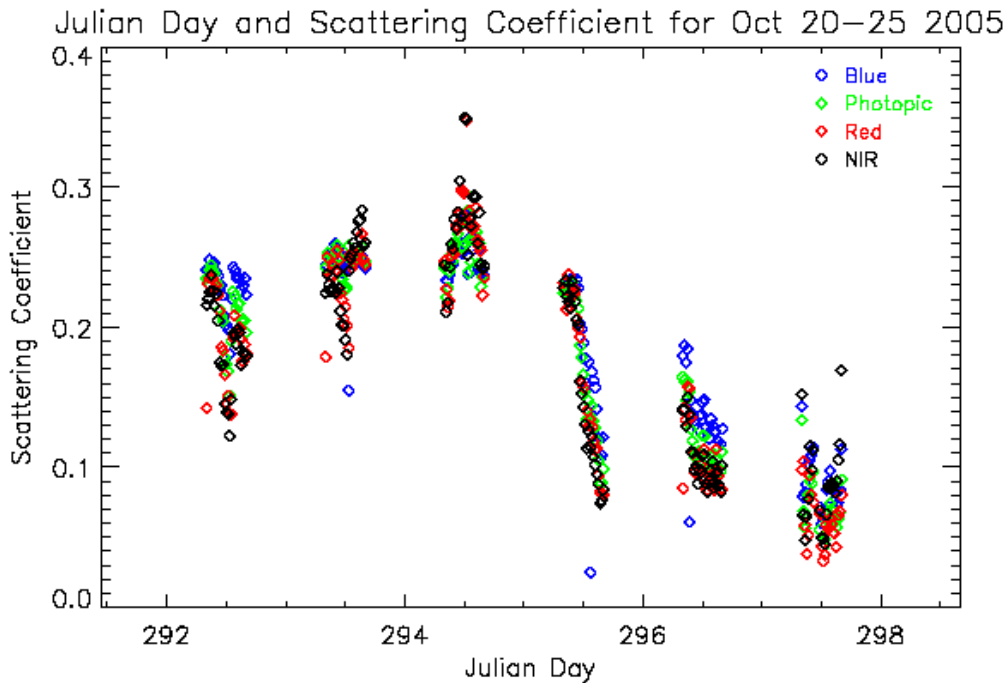


Figure 9-13.  Variation in scattering coefficient during the day (20 – 25 October 2005)

A comparison of the results in the different filters with those in the photopic filter is shown in Figure 9-14. In all cases, the spectral results correlate quite reasonably with the photopic results. We also note that general magnitudes are reasonable in all cases. All three filters have similar results to the photopic at high extinctions, where larger droplets should prevail and the results should be less spectrally dependent. At the low scattering coefficient end, with relatively clear air, and the scattering is higher in the blue and lower in the red and NIR, as expected.

It is also interesting that the correlation between the spectral results and the photopic results is somewhat poorer in the NIR than in the other filters. We speculate that this may have to do with variations in the drop size distribution under different conditions. The path of sight is approximately 9 - 10 m above sea level, and is subject to droplets kicked up by the surf zone. Even on relatively clear days, this path of sight may be more populated with large droplets than a typical maritime or continental air mass. Depending on the populations of these large droplets, we would anticipate potentially different scattering results in the NIR, in relation to the photopic.
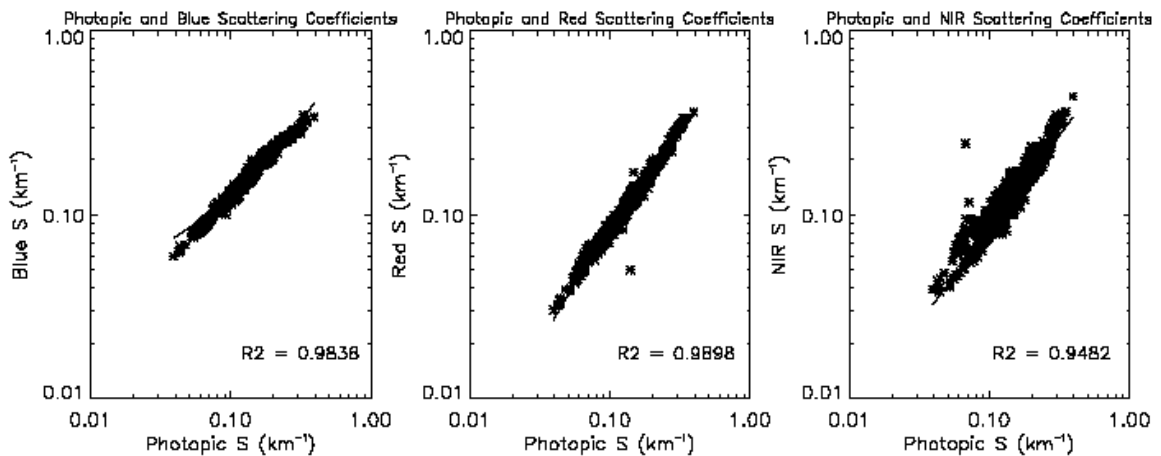


Figure 9-14. Correlation of scattering coefficients at different wavelengths

## 9.5 Comparison with Transmissometer

In addition to the MSI, the site was instrumented with several other instruments, including a transmissometer operating at 0.55 μm (nearly photopic) and a nephelometer operating in the photopic band. The transmissometers were operating over the same path of sight as the MSI, and the nephelometer was located near the MSI target box.

Figures 9-15 – 9-18 show records of the extinction and scattering coefficients measured with the transmissometer and MSI for four 7-day periods in August 2005. Since the MSI is presently limited to daylight operation, only the daytime values from the transmissometer are shown in these charts. The agreement between the two measurements is extremely good.
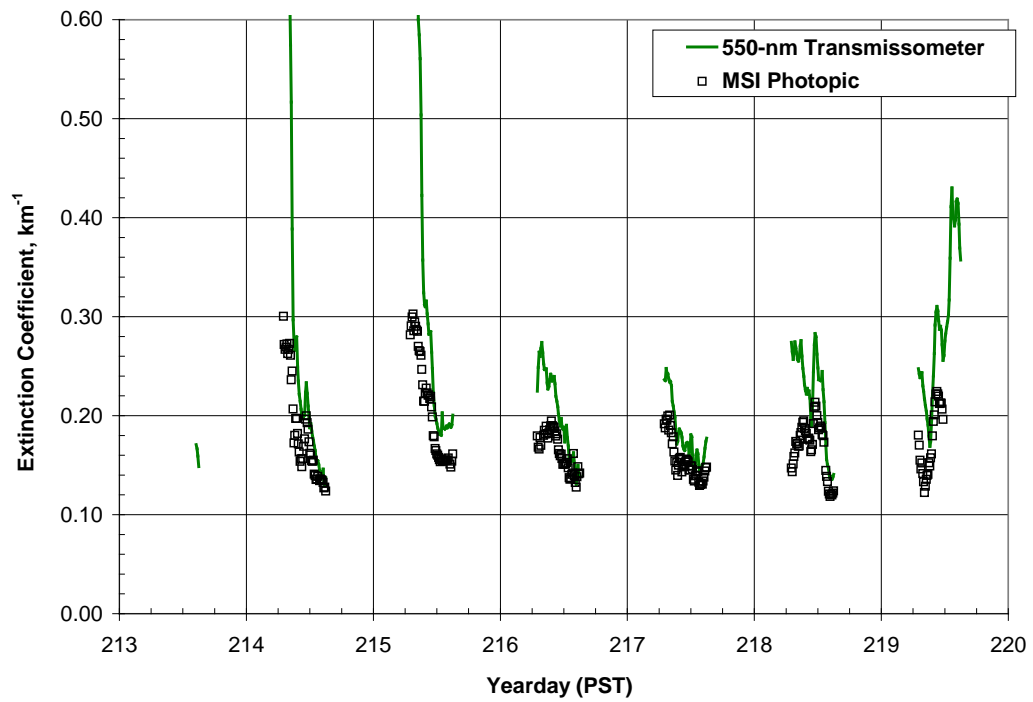
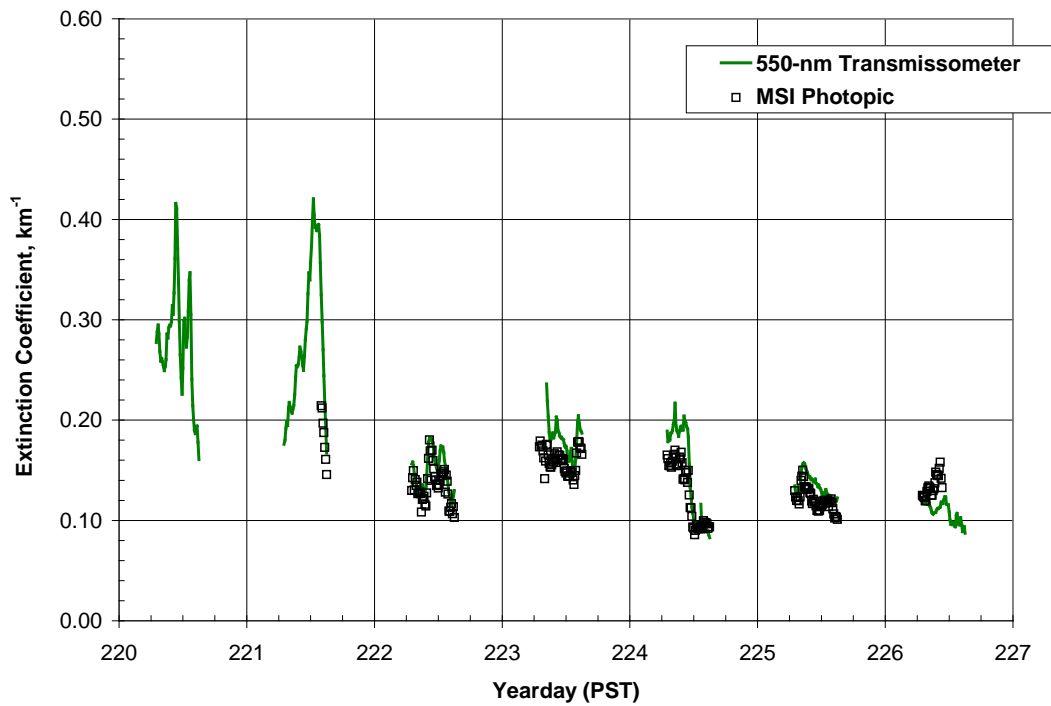Figure 9-15.    Record of MSI and 0.55-μm transmissometer measurements (1 – 7 August 2005)



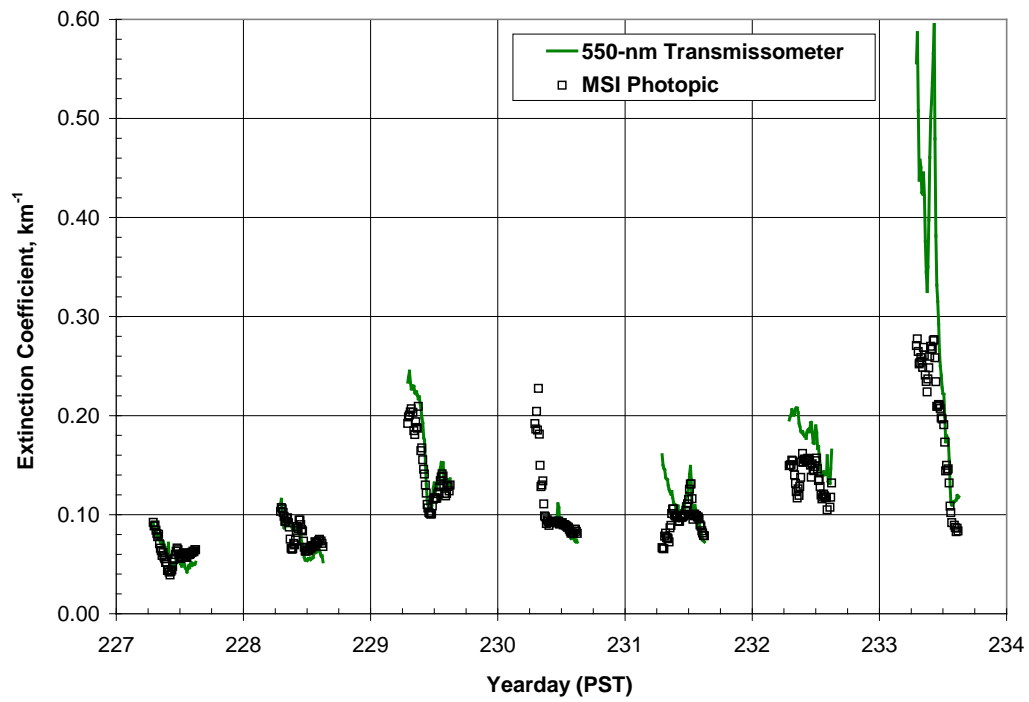Figure 9-16.    Record of MSI and 0.55-μm transmissometer measurements (8 – 14 August 2005)

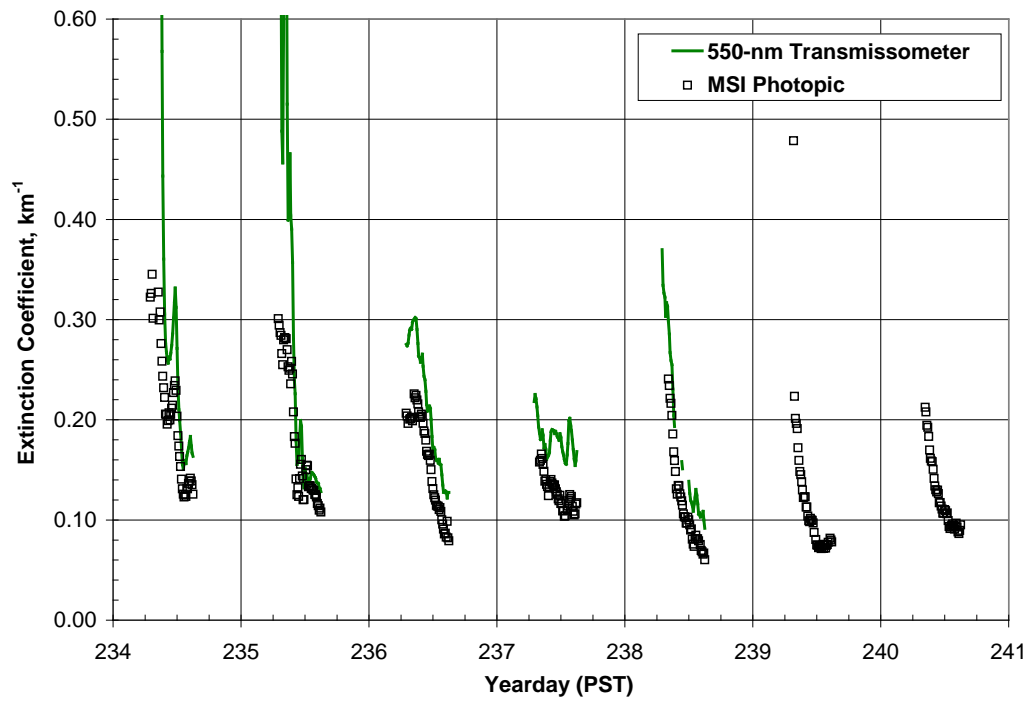Figure 9-17. Record of MSI and 0.55-μm transmissometer measurements (15 – 21 August 2005)



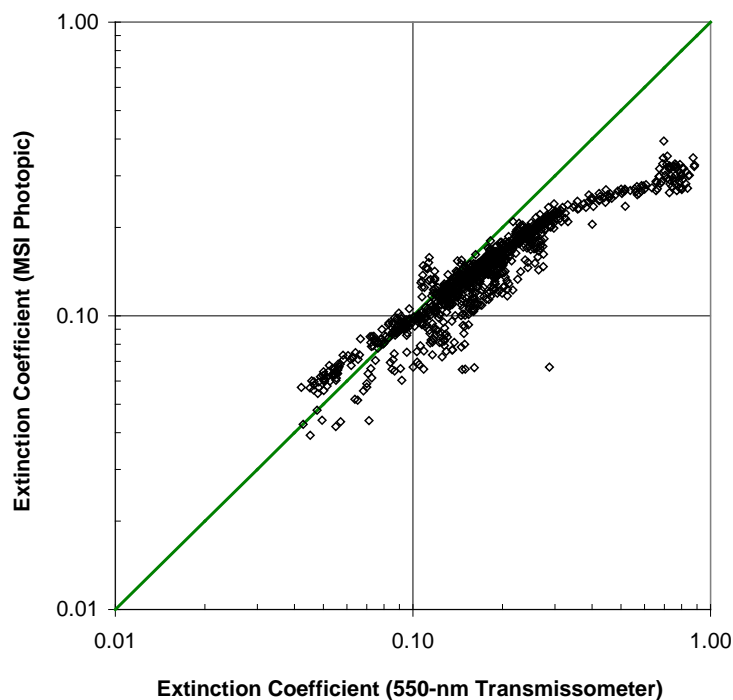Figure 9-18. Record of MSI and 0.55-μm transmissometer measurements (22 – 29 August 2005)

Figure 9-19. Scatter plot comparing MSI and 0.55-µm transmissometer data for August 2005

Figure 9-19 shows a scatter plot comparing the extinction measurements made with the MSI and the 0.55-µm transmissometer in August 2005. This plot confirms the agreement seen in the 7-day records – the correlation coefficient is 0.92 and most of the data fall near a line with unity slope. At times of high extinction (extinction coefficient $\geq 0.4$ km$^{-1}$), the transmissometer tends to report higher values than the MSI. There are two possible reasons for this behavior. First, at these high extinction levels, the transmission over the 7.07-km path is less than 6 % and small changes in the measured transmission (due to variations in the back-ground level) result in large errors in the calculated extinction coefficient. Second, at high extinction, measuring the contrast of the black box in the MSI image is affected by imperfections in the non-uniformity correction used in the image processing. Third, as shown in Figure 9-11, using the 1.6-degree slant path as the horizon might contribute to the roll-off at high extinction values.

Figures 9-20 and 9-21 show records of the extinction and scattering coefficients measured with the transmissometer and MSI for two 7-day periods in the fall of 2006. The agreement between the two measurements is extremely good. Figure 9-22 shows a scatter plot comparing the two measurements for this time period. This plot confirms the agreement seen in the 7-day records – the correlation coefficient is 0.84 and most of the data fall near a line with unity slope. Figures 9-22 shows that, on average, the MSI and transmissometer give the same results at low extinction values, as opposed to Figure 9-19, where the transmissometer tends to report lower extinction coefficients. The transmissometer was re-calibrated before this IOP, the alignment was adjusted more frequently, and background readings were taken regularly. At times of high extinction (extinction coefficient $\geq 0.4$ km$^{-1}$),

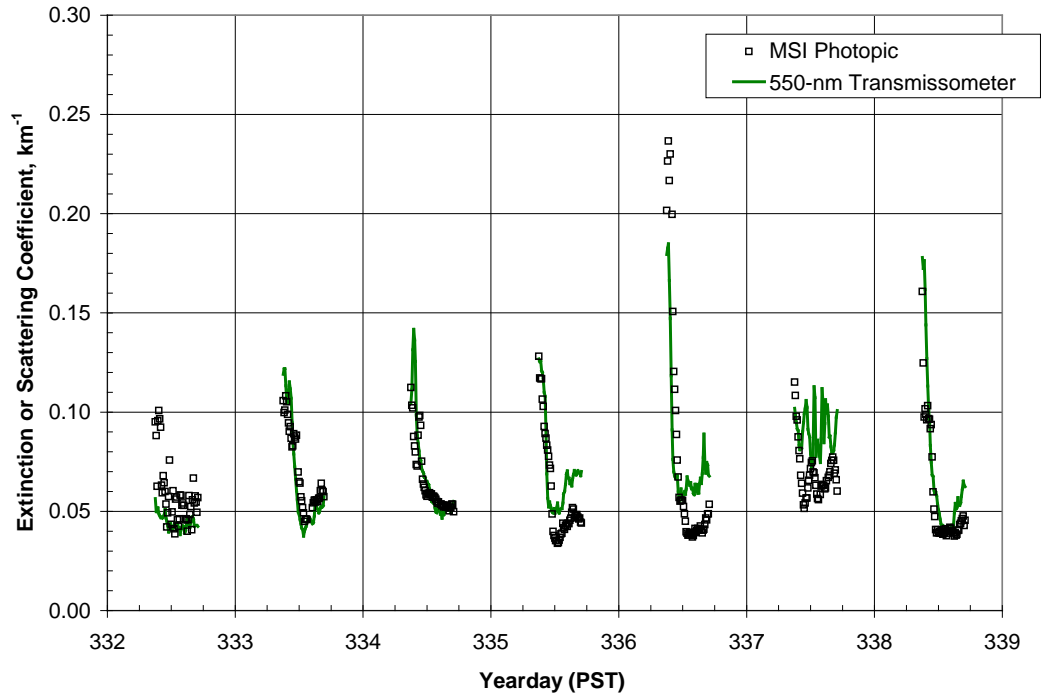we see the same trend as Figure 9-19 – the transmissometer reports higher values than the MSI.



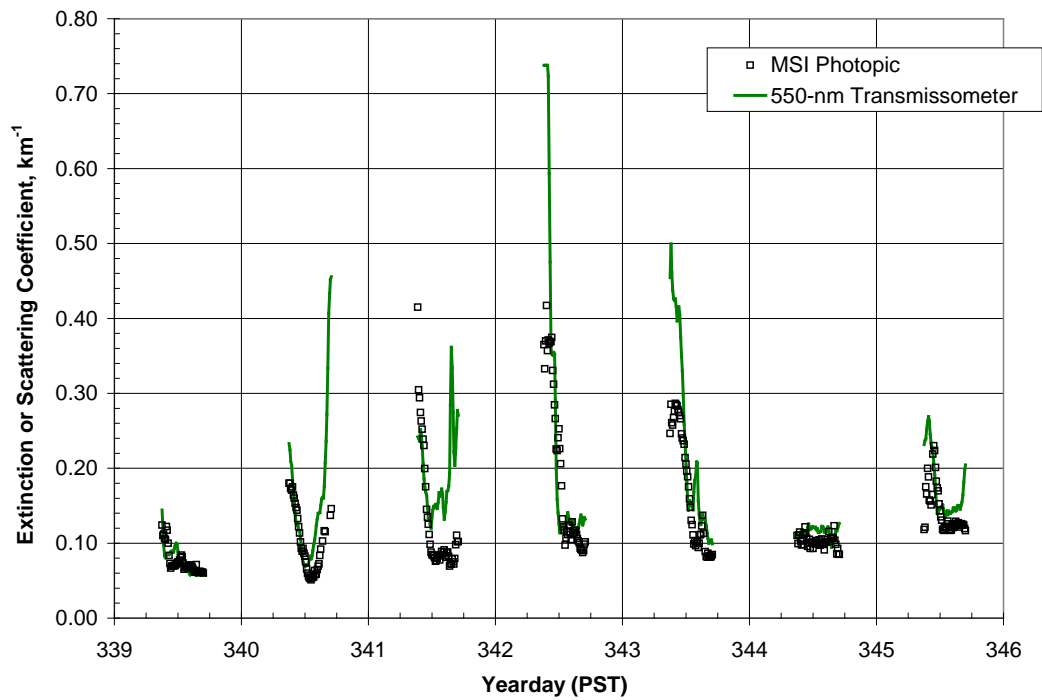Figure 9-20. Record of MSI and 0.55-μm transmissometer measurements (28 November 2006 – 4 December 2006)



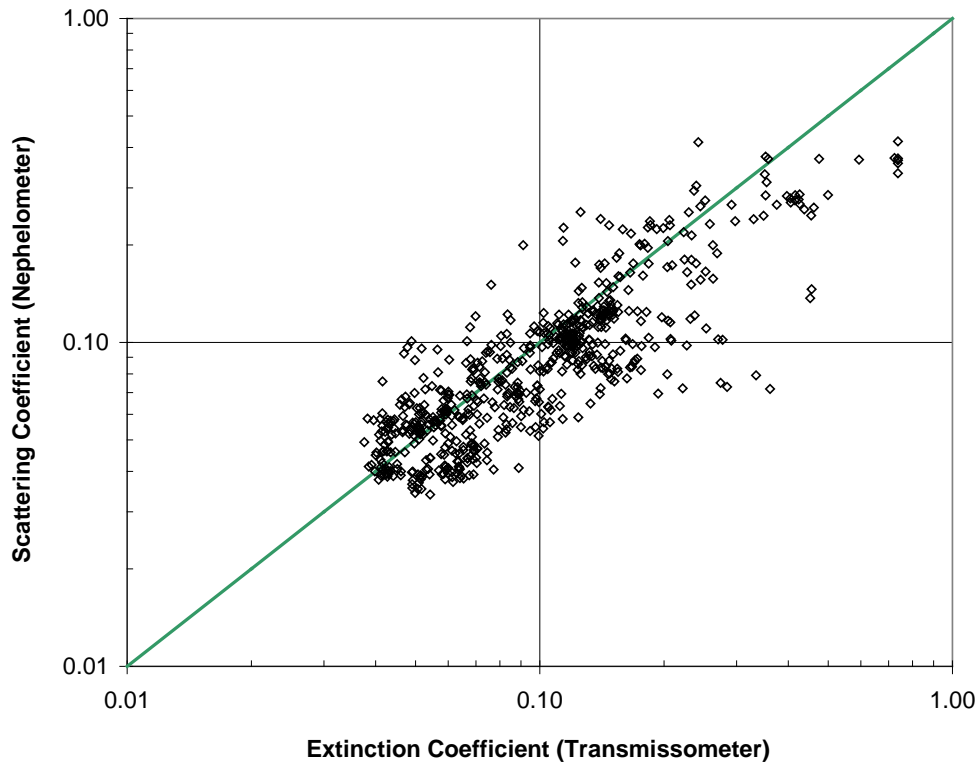Figure 9-21. Record of MSI and 0.55-μm transmissometer measurements (5 December 2006 – 11 December 2006)

Figure 9-22. Scatter plot comparing MSI and 0.55-μm transmissometer data for two-week period from 28 November to 11 December 2006

## 9.5 Potential for Future Development

For some applications, it would be useful to either measure or estimate the scattering coefficient along paths of sight in Short Wave IR (SWIR) wavelengths between 1 and 3 μm. One approach to this goal would be to design a SWIR MSI. We have not fully investigated this approach, but feel it may be a very fruitful approach. A second method would be to use a visible MSI, and use the multi-spectral nature of the measurements to provide an estimate of the SWIR scattering, either empirically or using modeling. Although extensive modeling of this approach was beyond the scope of this work, we have evaluated the SWIR extinction measurements in relation to the MSI data. Figure 9-23 shows a scatter plot of SWIR extinction, derived from the SSC-SD transmissometer, as a function of the photopic MSI scattering coefficient. We see from this figure that the photopic scattering coefficient measured by the MSI is a reasonable predictor of the SWIR extinction coefficient, particularly when the NIR/photopic ratio from the MSI is taken into account. There is surprisingly little scatter in this plot, and a simple curve fit, as a function of NIR/photopic ratio, would enable one to predict the approximate range of anticipated SWIR extinction from the visible data. This plot represents a very limited data set. Clearly more study would be required to determine whether, for applications requiring an estimate of the SWIR extinction, it is more productive to design a SWIR MSI or use a visible MSI and an empirical extrapolation to the SWIR. In particular, the direction of the non-linear behavior at high extinction values may be a measurement artifact. For example, perhaps the MSI with the fixed target at 7.2 km is not as accurate at the very high extinctions. We do not expect this to

be so much an issue with later versions of the MSI, which will have targets at a variety of ranges. In choosing between measuring in the visible and the SWIR, we also need to be aware that SWIR sensors tend to have higher noise and non-uniformity; however they may be sufficiently accurate for some MSI applications.
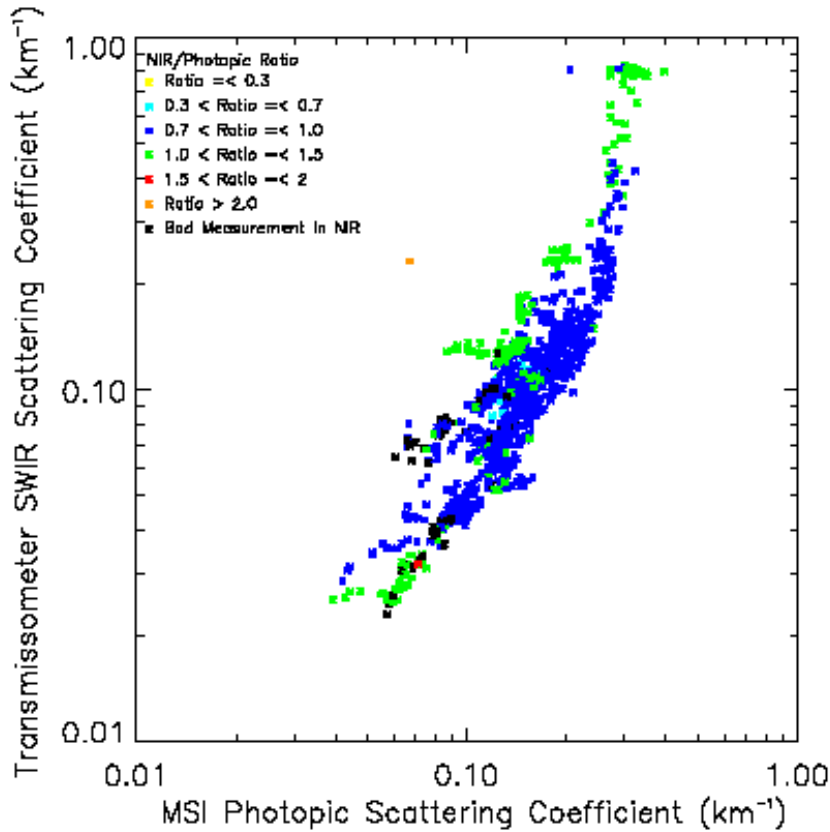


Figure 9-23. Extinction coefficient at 1.06 mm, from SSC transmissometer, versus MSI photopic scattering coefficient, color-coded by NIR/photopic ratio

Based on the work reported here, we believe that the MSI is mature enough to support development of systems for use in field operations. For this application, we would no longer use the black target used in this experimental setup. Potential optical targets of opportunity include dark landscape features, open doors and other dark objects in an urban environment, and the air/sea interface as well as ocean radiant characteristics in ocean environments. The MSI technique depends in large part on the accuracy of the measurements and algorithm, but it also depends on having a reasonably well-known optical target. Clearly studies of the natural variations in targets of opportunity (as a function of wavelength) would be important in isolating the most useful targets of opportunity. For example, we would anticipate that some directions and wavelengths will have higher air/sea interface contrast than others; those with inherent contrast closest to negative one will yield the most accurate extinction results. The impacts of using these less optimal targets on the overall system accuracy can be derived using system sensitivity studies, such as were done with the HSI [Ref. 9-18]. We feel that development of a SWIR or IR system, in conjunction with further hardening of the visible

MSI system, should enable development of field systems for operational use in the future. Although a field hardened system may be slightly less accurate than the current system, it should be far more accurate than any other approach of we are aware for determining the scattering over an extended path from a single location.

## 9.6 Conclusions

A new system, the Multispectral Scattering Imager or MSI, has been developed to measure extinction coefficients over extended paths. This system measures the extinction coefficient and visibility range in the blue, green, red, and NIR wavelengths, and can be adapted to other wavelengths. In the visible, these extinction coefficients may be used as a close estimate of the scattering coefficients, under most conditions. The MSI photopic band results correlated very well with results from a 0.55-μm transmissometer. The data appear to vary reasonably as a function of spectral band. The images also provide a convenient means to visually verify the conditions that were occurring at the time of the measurements. The results compare very well with scene weather as evaluated from visual inspection of the imagery.

The current system is limited to daytime operation. Although we have developed the theory for extracting visibility at night from data such as that acquired by the MSI, we did not develop the programs and specific methodology to process nighttime data for this project.

The primary limitation on the system as fielded is path uniformity. The path extinction does not have to be constant as a function of azimuth angle, but an overall effective extinction will be determined if it varies as a function of range. However, if such a change in range is caused by clouds in the path of sight, the instrument can be expected to identify this situation. If fielded on a ship, we would need to explore the limitations due to the uncertainty in inherent contrast. Accuracy of the measurements is also important, and we have not yet determined whether we could use less accurate or stable cameras, or less accurate calibrations.

The MSI has a number of attractive features for supporting extended atmospheric measurement campaigns or in future use as a decision aid for military systems. First, it provides integrated-path measurements, but only requires an active element at one end of the path. It is a passive system appropriate for covert use. Second, the system alignment is robust – the image processing algorithm can find the darkest pixels corresponding to the reference target and compensate for alignment errors due to mechanical disturbances or atmospheric refraction. Third, the system was extremely reliable. Data sets were acquired every 10 minutes, except for one drive failure and occasional data loss due to power failures.

Experience with this system also points out what is important in any future development efforts: optimizing the optical coatings for the measurement bands, eliminating fiber optic taper in the optical system and use of a camera with high spatial uniformity and no/few bad pixels, characterizing the inherent contrast of the black target, and using a path for the region of interest defined as "horizon" that is as close to the target path as possible. All of these design principles would need to be implemented in an instrument designed for atmospheric science studies, where accurate measurements are needed over an extinction range from 0.01 to > 2 km$^{-1}$. In addition, since path uniformity is important for accurate measurements, a sky imager should be used in conjunction with the visibility sensor in atmospheric science studies to validate or reject measurements depending on the path

uniformity. Some of these design principles could be relaxed in an instrument designed to support high-energy laser missions, where accurate measurements are needed only over a limited range of extinction conditions, perhaps from 0.04 to 0.3 km-1, corresponding to 5-km transmission ranging from 0.82 to 0.22.

We are pleased with how far the MSI has come in this relatively short development time, and feel it has exceptional potential for the future.

**References**

9-1. H. Koschmeider, "Theorie der horizontalen Sichtweite", Beitr. Phys. frein Atmos. **12**, 33-53 (1924)

9-2. J. A. Curcio and K. A. Durbin, "Atmospheric Transmission in the Visible Region", Report 5368, Naval Research Laboratory, Washington, DC (1959)

9-3. W. C. Malm, G. Persha, R. tree, R. Stocker, I. Tombach, and H. Iyer, "Comparison of Atmospheric Extinction Measurements made by a Transmissometer, Integrating Nephelometer, and Teleradiometer with Natural and Artificial Black Target", Air Pollution Control Association Specialty Conference, Grand Teton National Park, Wyoming, 7 – 10 September 1986

9-4. R. W. Johnson, W. S. Hering, and J. E. Shields, *Automated Visibility and Cloud Cover Measurements with a Solid State Imaging System*, University of California, San Diego, Scripps Institution of Oceanography, Marine Physical Laboratory, SIO 89-7, GL-TR-89-0061, NTIS No. ADA216906, 1989.

9-5. J. E. Shields, R. W. Johnson, and M. E. Karr, *An Automated Observing System for Passive Evaluation of Cloud Cover and Visibility*, University of California, San Diego, Scripps Institution of Oceanography, Marine Physical Laboratory, SIO 92-22, PL-TR-92-2202, 1992.

9-6. R. W. Johnson, T. L. Koehler, and J. E. Shields, *A Multi-Station Set of Whole Sky Imagers and A Preliminary Assessment of the Emerging Data Base*, Proceedings of the Cloud Impacts on DOD Operations and Systems, 1988 Workshop, pp. 159 – 162 1988.

9-7. J. E. Shields, R. W. Johnson, and T. L. Koehler, *Automated Whole Sky Imaging Systems for Cloud Field Assessment*, Fourth Symposium on Global Change Studies, American Meteorological Society, 1993.

9-8. J. E. Shields, R. W. Johnson, M. E. Karr, and J. L. Wertz, *Automated Day/Night Whole Sky Imagers for Field Assessment of Cloud Cover Distributions and Radiance Distributions*, Tenth Symposium on Meteorological Observations and Instrumentation, American Meteorological Society, 1998

9-9. J. E. Shields, R. W. Johnson, M. E. Karr, A. R. Burden, and J. G. Baker, *Whole Sky Imagers for Real-time Cloud Assessment, Cloud Free Line of Sight Determinations and Potential Tactical Applications*, The Battlespace Atmospheric and Cloud Impacts on Military Operations (BACIMO) Conference, Monterey, CA, 2003

9-10. J. E. Shields, R. W. Johnson, M. E. Karr, A. R. Burden, and J. G. Baker, *Daylight Visible/NIR Whole Sky Imagers for Cloud and Radiance Monitoring in Support of UV Research Programs*, International Symposium on Optical Science and Technology, SPIE the International Society for Optical Engineering, 2003

9-11. J. E. Shields, J. G. Baker, M. E. Karr, R. W. Johnson, and A. R. Burden*, Visibility measurements along extended paths over the ocean surface,* International Symposium on Optical Science and Technology, SPIE the International Society for Optical Engineering, August 2005

9-12. R. W. Boyd, *Radiometry and the Detection of Optical Radiation*, a volume in the Wiley Series in Pure and Applied Optics, S. S. Ballard Founder, J. W. Goodman Advisory Editor, John Wiley & Sons, New York/Chichester/Brisbane/Toronto/Singapore (1983)

9-13. R. McCluney, *Introduction to Radiometry and Photometry*, Artech House, Boston, London (1994)

9-14. E. J. McCartney, *Optics of the Atmosphere*, a volume in the Wiley Series in Pure and Applied Optics, S. S. Ballard Advisory Editor, John Wiley & Sons, New York/London/Sydney/Toronto (1976)

9-15. S. Q. Duntley, A. R. Boileau, and R. W. Preisendorfer, *Image Transmission by the Troposphere I\**, Journal of the Optical Society of America, Vol. 47 No. 6 499-506 (1957)

9-16. K. N. Liou, *An Introduction to Atmospheric Radiation*, International Geophysics Series Volume 26, Academic Press, New York, London, Toronto, Sydney, San Francisco (1980)

9-17. Glossary of Meteorology, Edited by R. E. Huschke, American Meteorological Society, Boston, (1959, reprinted 1998)

9-18. J. E. Shields, R. W. Johnson, and M. E. Karr, A Sensitivity Study of Daytime Visibility Determination with a Horizon Scanning Imagery, University of California, San Diego, Scripps Institution of Oceanography, Marine Physical Laboratory, SIO 91-15, PL-TR-91-2189, 1991